CFD Letters 13 Issue 1 (2021) 84-95

Penerbit Akademia Baru

CFD Letters

Journal homepage: www.akademiabaru.com/cfdl.html
ISSN: 2180-1363

CFD Application for Solid Propellant Rocket Simulation: A Review

Ali Almayas[1], Mohd Saffuan Yaakob[1], Faieza Abdul Aziz[2], Noorfaizal Yidris[1,3], Kamarul Arifin Ahmad[1,3,*]

[1] Department of Aerospace Engineering, Faculty of Engineering, Universiti Putra Malaysia, 43400 Serdang, Selangor, Malaysia
[2] Department of Mechanical Engineering, Faculty of Engineering, Universiti Putra Malaysia, 43400 Serdang, Selangor, Malaysia
[3] Aerospace Malaysia Research Centre, Faculty of Engineering, Universiti Putra Malaysia, 43400 Serdang, Selangor, Malaysia

ARTICLE INFO

Article history:
Received 23 November 2020
Received in revised form 18 January 2021
Accepted 23 January 2021
Available online 31 January 2021

ABSTRACT

The design and testing processes of Solid Propellant Rocket should be done properly to ensure it safe to be used. Prototype testing involve in experimental method to test Solid Propellant Rocket. Few prototypes needed to clarify all the errors because it need to be test several times. It is a time-consuming and cost-consuming process when using experimental method. Other than that, analytic method can be used to solve the engineering problem. Even though the method is difficult and complicated, it has been proven as reliable tools to assists experimentation. Computational Fluid Dynamics (CFD) tool has been used as part of the design tool since the beginning of its existence. This is due to the fact that the tool is cheap but with acceptable accuracy and can be used without any safety issue. This review paper presents a comprehensive coverage on the application of CFD in the solid propellant rocket research. This is an important review as to provide a guideline to the new researchers that want to start research work in this area. This paper will give an insight on the research path and tools that can be used to assist the researchers on their research work.

Keywords:
Solid propellant rocket; solid rocket simulation; computation fluid dynamics

1. Introduction

Solid Propellant Rocket Motor (SRM) is a non-trivial part in aerospace technology. It is not a new technology but very reliable and being used as part of the space rocket launching around the world. The rocket motor is a fundamental piece of a rocket that used to boost a rocket [1]. It comprises of a case, insulator, cap, nozzle, igniter, and so forth. It works utilizing standards, for example, pressure vessels since it stores the fuel. Rocket motor working conditions could be in high temperature and pressure [2].

The rocket motor case design relies on the inside pressure factor and material been used. A thick-walled chamber been used for high internal pressure area in rocket motor case.

---

[*] *Corresponding author.*
E-mail address: aekamarul@upm.edu.my (Kamarul Arifin Ahmad)

https://doi.org/10.37934/cfdl.13.1.8495

The higher yield strength of the materials, the thinner walled chamber can be used in the rocket motor design [3]. To ensure the success and safety of the SRM, the design and testing processes should be done thoroughly. Computational Fluid Dynamics (CFD) tool has been used as part of the design tool since the beginning of its existence. This is due to the fact that the tool is cheap but with acceptable accuracy and can be used without any safety issue. Recent progress in numerical approach and computing power also contribute to the accuracy of CFD results [4].

Nozzle simulation by using Computational Fluid Dynamics (CFD) Nozzle is the most important part in rocket, it converts the low velocity, high pressure, high temperature gas in the combustion chamber into high velocity gas of lover pressure and temperature. Computational Fluid Dynamics is an engineering tool that assists experimentation. Its scope is not limited to fluid dynamics, CFD could be applied to any process which involves transport phenomena with it. To solve an engineering problem, we can make use of various methods like the analytical method, experimental methods using prototypes. The analytical method is very complicated and difficult. The experimental methods are very costly. If any errors in the design were detected during the prototype testing, another prototype is to be made clarifying all the errors and again tested. This is a time-consuming as well as a cost-consuming process. The introduction of Computational Fluid Dynamics has overcome this difficulty as well as revolutionized the field of engineering. In CFD a problem is simulated in software and the transport equations associated with the problem is mathematically solved with computer assistance. Thus, we would be able to predict the results of a problem before experimentation.

The purpose of this review paper is to present a comprehensive coverage on the application of CFD in the solid propellant rocket research. This is an important review as to provide a guideline to the new researchers that want to start research work in this area. This paper will give an insight on the research path and tools that can be used to assist the researchers on their research work.

2. Main Categories of CFD Studies

2.1 Burning of the Propellant

Theoretical studies of heterogeneous solid rocket propellant combustion been difficult since burning of a heterogeneous solid rocket propellant generate a complex flame structure [5]. In the gas phase, three separate flames can be identified such as

i. Primary flame between the decomposition products of the binder and the oxidizer
ii. Premixed oxidizer flame
iii. Final diffusion flame between the products of the other two flames

In one-dimensional combustion studies, it essentially omits or fails to appropriately account for important physics, yet endeavours to account lot of the significant feature of the combustion field. Several improvements to steady-state burning have been conducted. Lee *et al.,* [6] presented a modified picture for the flame structure for AP-Binder-AP sandwich as shown in Figure 1. The figure shows the combustion zone standards, comprises of a Leading-Edge Flame (LEF) that remains in the blending region of the oxidizer and fuel vapours, and a diffusion flame that trails from the LEF to a limited extent where the fuel vapor is completely burned-through. The LEF is an area of extremely high heat discharge when contrasted to the rest of the diffusion flames and contributes the greater part of the heat transfer back of the propellant surface [7]. This edge happens when temperature there being too low causing the diffusion flame unable to extend all the way to the surface.

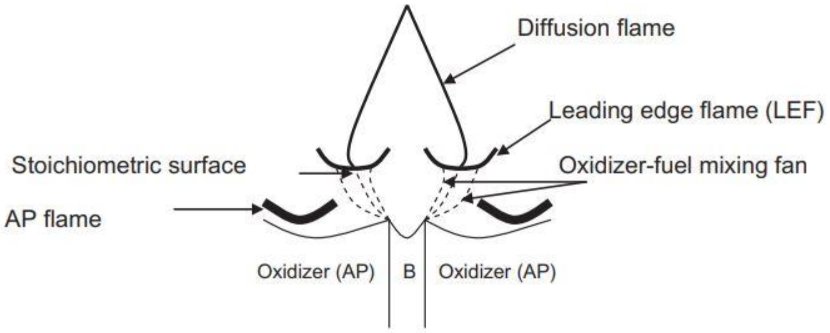

Fig. 1. Flame structure for an AP-Binder-AP sandwich [6]

The propellant burning rate, in its easiest structure, is the rate of conversion of solid to gas in a toward normal to a planar burning surface. The Saint Robert-Vieille law is regularly used to describe the burning rate over restricted ranges of pressure

$$r = bp^n$$

where r is the linear burning rate; p is the pressure; n is the burning rate pressure exponent; and b is the constant of proportionality. The affectability of the burning rate to changes in pressure increments as an approaches solidarity and can cause rocket motor performance to endure. In spite of the fact that not a cause of combustion instability, a change in the burning rate pressure exponent may advance precariousness. Linear theory predicts that acoustic driving should increment as the burning rate exponent increases [8]. Little changes in the motor operating pressure at $n = 1$ will result in enormous changes in the burning rate and may prompt to a hazardous event, for example, motor failure.

Typically, the Saint Robert-Vieille law does not hold over a wide pressure range, and solid rocket propellants will show a "slope break" or change in the burning rate pressure exponent at a characteristic pressure, $p*$, where the burning rate changes from a lower to a higher value. The "slope break" is regularly seen in AP-based propellants at pressure over 14 MPa. The area of $p*$ is a basic ballistic design parameter. In a perfect world, rocket motor working pressures ought not cover with a break in the burning rate pressure exponent.

2.2 Plume Phenomenon

The plume is recreated as a two-phase flow, a gas phase and a particle phase. A few approximations are made in order to simplify the investigation and decrease the computational cost of the simulation [9]. The plume is thought to be at steady state, axisymmetrical, non-turbulent and non-reactive as the gas mean free-path is low a result of the low gas density. Inside the flow, alumina particles and the gas may have various speeds and temperature distributions. Besides, as there are a few sizes of particles, each size class is associated with its own thermo-physical properties. For each phase, the tackling of the flow field is controlled by the mass, momentum and energy conservation equations. Momentum and energy trades among gas and particles incite source terms to the equations of each phase.

2.2.1 Gas phase modelling (without the condensed process)

The gas flow field is recreated utilizing a code which solves the compressible Navier-Stokes equations for a multi-species gas using a finite volume method. The Knudsen number which characterizes the flow regime, is sufficiently low in most of the flow field to enable the simulation of the main core of the plume with a continuum approach. In the region with relatively high Knudsen number, an alternative approach would be more appropriate to simulate the flow field taking into account rarefaction aspects. However, in the plume, these areas are located in the backstream region above the nozzle lip and in the diffuse shock wave between the atmosphere and exhaust gases. Even if the temperature is quite high in these regions, the gas is rarefied and there are nearly no particles, so that they would not contribute significantly to the heat fluxes at the body of the vehicle nor the global radiation in the flow field.

The gas phase is composed of Nm different species and the diffusion between the exhaust gases coming from the nozzle and the free-stream gases of the atmosphere is taken into account. The governing equations as discussed by Oliver [10], can be written as

$$\frac{\partial Q}{\partial t} + \nabla . F_c = \nabla . F_d + S_g \tag{1}$$

where Q is the vector of conserved quantities, F_c is the vector of convective fluxes, F_d the vector of diffusive fluxes and S_g the vector of source terms due to radiation and gas/particle interaction. Those vectors are given by

$$Q = \begin{pmatrix} \rho Y_i \\ | \\ \rho Y_{N_m} \\ \rho u \\ \rho e_t \end{pmatrix}, F_c = \begin{pmatrix} \rho Y_i \\ | \\ \rho Y_{N_m} u \\ \rho u \otimes \quad u + PI \\ \rho \left(e_t + \frac{P}{\rho} \right) u \end{pmatrix},$$

$$F_d = \begin{pmatrix} -J_1 \\ | \\ -J_{N_m} \\ \tau \\ \tau . u - J_e \end{pmatrix}, S_g = \begin{pmatrix} 0 \\ | \\ 0 \\ S_d \\ S_e + P_{rad} \end{pmatrix}, \tag{2}$$

where ρ is the density of the gas, Y_i is the mass fraction of molecular species i, u is the hydrodynamic velocity of the gas and e_t is the specific total energy of the gas. Thermodynamic equations of state permit to pass from the conservative quantities to the natural quantities, the pressure P and temperature T.

$$\rho e_t = \frac{1}{2} \rho u^2 + \sum_{i=1}^{New} \rho Y_i e_{int}^i (T),\ P = \sum_{i=1}^{New} \rho Y_i \frac{RT}{M_i},$$

$$e_{int}^i (T) = e_{int}^i (T_0) + \int_{T_0}^{T} c_v^i (T) dT, \tag{3}$$

where R is the universal gas constant, M_i the molar mass of species i, e_{int} I its internal energy and c_v^i (T), its specific heat calculated as a polynomial function of the temperature. In the diffusive fluxes vector, the diffusion flux Ji is calculated according to the Fick's Law as

$$J_i = -\rho D_i \nabla Y_i, \tag{4}$$

where D_i is the diffusion coefficient of the species i calculated with a Schmidt number equal to one. τ is the viscous stress tensor for which the dynamic viscosity of each species is calculated with the Sutherland law. J_e stands for the energy diffusion vector which includes the conductive heat flux calculated with the Fourier law, and the molecular diffusion fluxes as

$$J_e = -\lambda_g \nabla T + \sum_{i=1}^{New} h_i J_i, \tag{5}$$

where λ_g is the thermal conductivity of the fluid and h_i the specific enthalpy of the species i. In the source term vector, S_d and S_e components are relative to momentum and convective exchanges between gas and particles, respectively. To solve these equations, used the finite volume method with a first order implicit scheme for the temporal integration, a second order scheme for space integration and an HLLC type scheme (Harten-Lax-van Leer Contact wave) [11] for the calculation of the convective fluxes between cells.

2.2.2 Condensed phase modelling

To simulate the particle phase, we use a Eulerian finite volume solver. The condensed phase is modelled by Nc classes of spherical particles, each class k having its own characteristic diameter D(k), temperature $T_p^{(k)}$, a number density of particles n(k), a volume fraction α (k), a mean velocity v (k) and a specific internal energy $e_{int}^{(k)}$. As for the fluid, for each class, the evolution of those variables is ruled by their own conservation equations. Note that each class is inert toward the others, and only the gas phase and radiation influence its evolution.

The temperature non-uniformity during particle solidification was discussed in References [12,13] for relatively large particles. However, for the small alumina particles considered in this work, it can be easily shown that the conductive time scale of a given particle is small compared to convective and radiative time scales, and to the residence time of the particles in the plume. It is therefore reasonable to consider isothermal particles in the present application. The system of governing equations for a particle class k can be written as

$$\frac{\partial Q_p^{(k)}}{\partial t} + \nabla . F_p^{(k)} = S_p^{(k)}, \tag{6}$$

where $Q_p^{(k)}$ is the vector of conserved quantities, $F_p^{(k)}$ the vector of convective fluxes and $S_p^{(k)}$ the source term vector. These vectors take the form of

$$Q_p^{(k)} = \begin{pmatrix} n^{(k)} \\ \alpha^{(k)}\rho_{Al} \\ \alpha^{(k)}\rho_{Al}V^{(k)} \\ \alpha^{(k)}\rho_{Al}e_{int}^{(k)} \end{pmatrix}, F_p^{(k)} = \begin{pmatrix} n^{(k)}v^{(k)} \\ \alpha^{(k)}\rho_{Al}v^{(k)} \\ \alpha^{(k)}\rho_{Al}V^{(k)}\otimes v^{(k)} \\ \alpha^{(k)}\rho_{Al}e_{int}^{(k)}v^{(k)} \end{pmatrix}$$

$$S_p^{(k)} = \begin{pmatrix} 0 \\ 0 \\ n^{(k)} F_{dr}^{(k)} \\ \alpha^{(k)} \rho_{Al} e_{int}^{(k)} \end{pmatrix}, \tag{7}$$

Here, ρ_{Al} is the density of alumina (assumed a constant equal to 2700 kg m^{-3}), $F_{dr}{}^{(k)}$ and $\varphi_c{}^{(k)}$ are respectively the drag force and the convective heat flux caused by the gas on a particle, and $P_{rad}{}^{(k)}$ the radiative power only due to the class k.

The alumina particles solidify following a supercooling process, that is to say, during its cooling along the plume, they remain in liquid state above the temperature of nucleation T_c of 1930 K. When a particle reaches this temperature, it starts to solidify at a constant temperature Tm of 2289 K, the melting temperature of alumina. Once totally solidified, the particle temperature decreases again due to radiative and convective cooling. A modelling of this phenomenon has been developed and allows us to express the internal energy $e_{int}{}^{(k)}$ of a class *k* as a bijective function of its temperature $T_p{}^{(k)}$ and its mass fraction of solid-state phase $\chi^{(k)}$.

$$\left\{\begin{matrix} e_{int}^{(k)}\left(X^{(k)}, T_p^{(k)}\right) = X^{(k)} c_{p,sol}(T_p^{(k)}) T_p^{(k)} \\ + (1 - X^{(k)})[L_{fus} + c_{p,liq}(T_p^{(k)}) T_p^{(k)} \\ e_{sol} = c_{p,sol}(T_m) T_m \\ e_{liq} = c_{p,liq}(T_c) T_c + L_{fus}, \end{matrix}\right\} \tag{8}$$

latent heat of fusion L_{fus}, where equal to 1.07 10^6 J/kg, $c_{p,liq}$ is the specific heat of liquid alumina (when a constant assumed equal to 1850 J/kg/ K) and $c_{p,sol}$, the specific heat of solid alumina that can be expressed as a polynomial function of the temperature. With this modelling, the particle is totally liquid if e_{int} is above e_{liq}, and totally solid when e_{int} is below e_{sol}. When a liquid particle reaches T_c, it undergoes a spontaneous partial crystallization and its temperature instantaneously changes to the melting temperature T_m while its internal energy remains conserved. In the plume, the heat created during the solidification of the alumina compensates with the cooling caused by interaction with the gas phase and by radiation. The phase change of alumina plays an important role not only to establish the correct temperatures of alumina in the plume but also because the radiative properties of alumina are different depending on its phase state. Moreover, the supercooling phenomenon tends to decrease the convective heat transfer between gas and particles, as the liquid particles are colder than the melting temperature and so slows down the cooling of alumina particles.

To solve the system of conservation equations for the condensed phase, we used a second order explicit scheme for the temporal integration, a second order spatial scheme and a Godunov [14] type scheme for the calculation of the fluxes at the faces of the mesh cells.

2.3 Interaction Between the Propellant Combustion and Flame

The momentum and energy exchanges between the gas phase and the particles are important for an accurate simulation of the flow field as they determine the cooling of alumina particles during the expansion of the plume. Because of the rarefied flow field, adequate modelling needs to be employed to evaluate momentum and energy exchange between both phases. Modelling suitable for highly compressible flows will be used.

The drag force $F_{dr}^{(k)}$ applied by the gas phase on a particle is responsible for momentum exchange between both phases, as discussed by Carlson and Hoglund [15], it is expressed as

$$F_{dr}^{(k)} = \frac{1}{8}\,\pi(D^{(k)})^2 \rho C_D \left\|u - v^{(k)}\right\|(u - v), \tag{9}$$

where C_D is the drag coefficient whose expression depends on the particle Reynolds number Rephased on the relative velocity and the dynamic viscosity μg of the gas by

$$Re_p = \frac{\rho D^{(k)}\left\|u - v^{(k)}\right\|}{\mu_e}, \tag{10}$$

For low Reynolds number as in plume flow field, Carlson and Hoglund [16] proposed the following expression of the drag coefficient

$$C_d = \frac{24}{Re_p}\left(1 + 0.15 Re_p^{0.687}\right) \times \frac{\left[1+\exp\left(-\frac{0.427}{M_p^{4.63}} - \frac{3}{Re_p^{0.88}}\right)\right]}{1+\frac{M_p}{Re_p}\left[3.82+1.28\exp\left(-1.25\frac{Re_p}{M_p}\right)\right]} \tag{11}$$

where Mp is the particle Mach Number based on the relative velocity of both phases. For highly compressible flows, Carlson and Hoglund [15] also developed in their work an expression of the convective heat transfer φc (k) given by the gas to a particle

$$\emptyset_c^{(k)} = \pi D^{(k)} Nu \lambda_g (T - T_p^{(k)}, \tag{12}$$

$$Nu = \frac{2+0.6 Re_p^{\frac{1}{2}} Pr^{\frac{1}{3}}}{\left[1+3.42\frac{M_p}{Re_p Pr}\left(2+0.6 Re_p^{\frac{1}{2}} Pr^{\frac{1}{3}}\right)\right]}, \tag{13}$$

where Nu is the Nusselt number expressed as a function of Re_p, M_p and Pr the Prandt number of the gas phase. In Eq. (2), the terms S_d and S_e are also related to $F_{dr}^{(k)}$ and $\varphi_c^{(k)}$ through the following expressions

$$S_d = -\sum_{k=1}^{Nc} n^{(k)} F_{dr}^{(k)},\ S_e = -\sum_{k=1}^{Nc} n^{(k)} \phi_c^{(k)}, \tag{14}$$

For the strong gas/particle coupling, we use the Lie splitting method [15] which consists of temporally integrating the source terms after a first calculation of transport phenomena

3. Modelling Approach

For academic reasons, the SRM is characterized as a cylindrical, circular-port duct with a circumferential porous surface canted at an angle α. Model in Figure 2(a) incorporates both the non-tapered and tapered geometries. This enables to account for the bulk flow originating from the non-tapered section of the motor. The origin for the coordinate system is placed at the interface where z and r denote the axial and radial coordinates, respectively (see Figures 2(b)). The non-tapered section of the cylindrical motor has dimensions of length L_0 and radius R_0. The gases are injected perpendicularly to the tapered surface. To satisfy mass conservation, the injected gases are forced to turn and merge with the bulk flow emerging from the parallel segment. The streamline behavior can be seen in Figure 2(a).

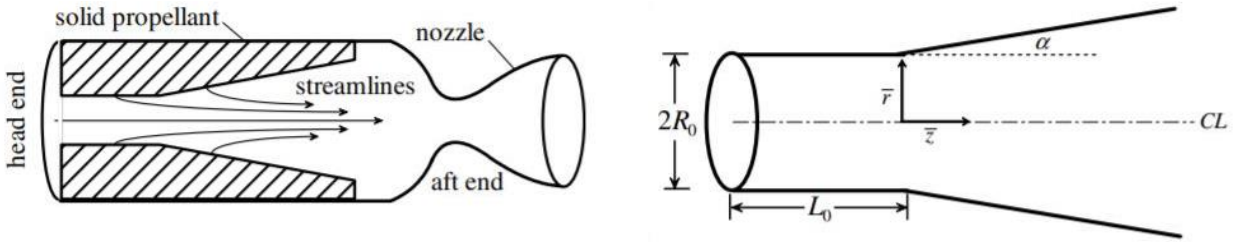

(a) (b)

Fig. 2. Schematic featuring a) typical cylindrical solid rocket motor with tapered bore and characteristic streamlines; and b) coordinate system for the mathematical model [10]

3.1 Governing Equation

For SRM simulation, vorticity is produced at the surface as a result of the interaction between the injected fluid and the axial pressure gradient; one may begin by obtaining the required form of the vorticity. Furthermore, the flow can be taken to be 1) axisymmetric, 2) inviscid, 3) incompressible, 4) rotational, and 5) nonreactive. In accordance with the stated assumptions, the kinematic equations of motion can be written in scalar notation. In the interest of clarity, these are

$$\bar{u}_r \frac{\partial \bar{u}_r}{\partial \bar{r}} + \bar{u}_z \frac{\partial \bar{u}_r}{\partial \bar{z}} = -\frac{1}{\rho}\frac{\partial \bar{p}}{\partial \bar{r}} \tag{15}$$

$$\bar{u}_r \frac{\partial \bar{u}_z}{\partial \bar{r}} + \bar{u}_z \frac{\partial \bar{u}_z}{\partial \bar{z}} = -\frac{1}{\rho}\frac{\partial \bar{p}}{\partial \bar{z}} \tag{16}$$

$$\bar{\Omega} = \bar{\Omega}_\theta = \frac{\partial \bar{u}_r}{\partial \bar{z}} - \frac{\partial \bar{u}_z}{\partial \bar{r}} = -\frac{1}{\bar{r}}\frac{\partial^2 \bar{\psi}}{\partial \bar{r}^2} - \frac{\partial}{\partial \bar{r}}\left(\frac{1}{\bar{r}}\frac{\partial \bar{\psi}}{\partial \bar{r}}\right) \tag{17}$$

where,

$$\bar{u}_r = -\frac{1}{\bar{r}}\frac{\partial \bar{\psi}}{\partial \bar{z}};\ \bar{u}_z = \frac{1}{\bar{r}}\frac{\partial \bar{\psi}}{\partial \bar{r}} \tag{18}$$

3.2 Boundary Conditions

While it is obvious that a radial velocity component exists at the interface, one should note that it does not add to the mass intersection into the tapered region; consequently, it is not needed to acquire a solution in the tapered domain as shown in Figure 3 below.

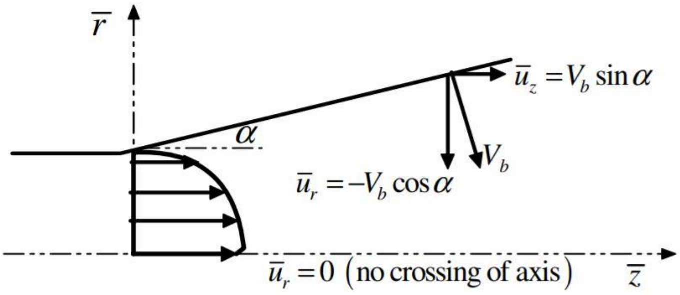

Fig. 3. Schematic of physical boundary conditions

The key limitations comprise of the accompanying: 1) the axial inflow condition emerging from mass equilibrium across the taper interface (representing for the bulk flow from the equal portion of the motor); 2) no stream across the centreline; and 3) uniform, orthonormal infusion at the burning surface. Numerically, the boundary conditions can be evaluated and expressed as

$$\left\{\begin{matrix} \bar{z} = 0, \forall\, \bar{r}, \bar{u}_z = \pi V_b \left(\frac{L_0}{R_0}\right) \cos(\frac{1}{2}\pi \bar{r}^2/R_0^2) \\ \bar{r} = \bar{r}_s, \forall\, \bar{z}, \bar{u}_z = \ -V_b \sin\alpha \\ \bar{r} = \bar{r}_s, \forall\, \bar{z}, \bar{u}_z = \ -V_b \cos\alpha \\ \bar{r} = 0, \forall\, \bar{z}, \bar{u}_r = 0 \end{matrix}\right\} \tag{19}$$

where V_b is the injection velocity at the burning surface.

3.3 Numerical Setup

3.3.1 Leading-order solution

At leading order, one obtains

$$\frac{\partial^2 \psi_0}{\partial r^2} - \frac{1}{r}\frac{\partial \psi_0}{\partial r} + \frac{4\beta_0^2 r^2}{r_s^4}\psi_0 = 0 \tag{20}$$

This is a simple, second-order, linear differential equation with the general solution

$$\psi_0(r,z) = C_1 \cos\left(\beta_0 \frac{r^2}{r_s^2}\right) + C_2 \sin\left(\beta_0 \frac{r^2}{r_s^2}\right) \tag{21}$$

Straightforward evaluation of Eq. (21) at the assigned boundary conditions gives

$$\psi_0(r,z) = \psi_s \sin\left(\beta_0 \frac{r^2}{r_s^2}\right) \tag{22}$$

where

$$\psi_s(z) = z \sec\alpha (1 + \frac{1}{2} z \tan\alpha) \ + L \ and\ \beta_0 = \frac{1}{2}\pi \tag{23}$$

It should be noted that at L = α = 0, one recovers

$$\psi_0(r,z) = z \sin(\beta_0 r^2) \tag{24}$$

Eq. (24) reproduces Culick's profile [14] for flow in an internal burning cylinder. The leading-order solution expressed by Eq. (22) may be referred to as an extended version of Culick's profile. This form is a result of the additional bulk flow caused by the increased surface area.

3.3.2 First-order solution

At first order, one obtains the following ordinary differential equation

$$\frac{\partial^2 \psi_1}{\partial r^2} - \frac{1}{r}\frac{\partial \psi_1}{\partial r} + \frac{4\beta_0^2 r^2}{r_s^4}\psi_1 + \frac{8r^2\beta_0\beta_1}{r_s^4}\psi_0 - \frac{8r^2\beta_0^2}{r_s^6}{\psi^2}_0 = 0 \tag{25}$$

with

$$\psi_1(0) = 0, \psi_1(r_s) = 0 \tag{26}$$

Applying these boundary conditions, one obtains

$$\psi_1(r,z) = \frac{\psi_s}{3r_s^2}\left[\begin{array}{c} 3\psi_s + \psi_s \cos\left(2\beta_0 \frac{r^2}{r_s^2}\right) - 2\psi_s \sin\left(\beta_0 \frac{r^2}{r_s^2}\right) - 4\psi_s \cos\left(\beta_0 \frac{r^2}{r_s^2}\right) \\ + 3\beta_1 r^2 \cos\left(\beta_0 \frac{r^2}{r_s^2}\right) \end{array}\right] \tag{27}$$

The first-order velocity ratio must be determined such that the nonslip condition is satisfied along the tapered surface. This can be written as

$$\nabla\psi_s \,.\, \hat{s} = \nabla\psi \,.\, \hat{s} = 0 \tag{28}$$

therefore,

$$\frac{\partial\psi}{\partial r}\cos\alpha + \frac{\partial\psi}{\partial z}\sin\alpha = (\psi_0 + \varepsilon\psi_1)_r \cos\alpha + (\psi_0 + \varepsilon\psi_1)_z \sin\alpha = 0 \tag{29}$$

Noting that ψ_0 already satisfies the no-slip condition at the wall, we recover

$$\frac{\partial\psi_1}{\partial r}\cos\alpha + \frac{\partial\psi_1}{\partial z}\sin\alpha = 0 \tag{30}$$

Again, it can be seen that the term containing sin α is negligibly small, being of O(ε). Setting Eq. (30) equal to zero and evaluating the resulting expression at the tapered surface, one obtains

$$\beta_1 = \frac{4\psi_s}{3r_s^2} \tag{31}$$

The required forms of the leading and first-order velocity ratios, β_0 and β_1, are presently known.

4. Issues and Recommendations

Despite the significant experience collected by the industry in designing solid rocket motors for space launchers and missiles, new developments require the physical phenomena to be more precisely understood, in order to guide the designer quickly towards less expensive and more reliable technical solutions. For that reason, CFD has gotten progressively important and more dependable to brings new knowledge into solid rocket propulsion. However, well-instrumented experiments will consistently be important to validate numerical simulations or dedicated models.

With available data, one can decide to determine the level of accuracy that is required and which physical boundaries are most important. The axial velocity profiles and the pressure drop are of paramount importance. However, the pursuit of a general expression that describes the flow field in tapered geometry requires that certain terms be neglected during the derivation process. To validate the dismissal of these terms, the same problem should solve mathematically.

5. Conclusions

Numerical methods used to simulate the internal flow fields existing in solid-rocket combustion chambers are sensibly useful for steady-state and transient flow conditions. Improvement could be refined by utilizing two-dimensional flow analyses. The uncertainties related with the prediction of the reaction of burning front advancement to such phenomena as mass flux, spin, un-symmetrical thermal gradients, and high-pressure transients seem to require first consideration, in spite of the fact solutions for a few or all of these uncertainties would be improved by two-dimensional analyses.

An impressive amount of motor and nozzle efficiency data has been amassed by the industry for contemporary plans. This data and experience have made it doable to change hypothetical explicit specific impulse and thrust coefficient values and to anticipate rather precisely the performance of new yet comparable motor designs. Demonstrated detailed analytical techniques are accessible for anticipating deliverable specific impulse and nozzle performance. These record for the major contributing variables to the momentum misfortunes experienced in solid rocket motors. At last, the act of scaling explicit specific impulse demonstrated in a ballistic assessment motor to that to be conveyed by a full-scale propulsion framework has demonstrated satisfactory in performance predictions.

Acknowledgement

This research was completed by using facility in the Faculty of Engineering, Universiti Putra Malaysia.

References

[1] Wibawa, Lasinta Ari Nendra. *Merancang Komponen Roket 3D dengan Autodesk Inventor Professional 2017*. Buku Katta, 2018.

[2] Emrich Jr, William J. *Principles of Nuclear Rocket Propulsion*. Butterworth-Heinemann, 2016. https://doi.org/10.1016/B978-0-12-804474-2.00012-6

[3] Wibawa, Lasinta Ari Nendra, Kuncoro Diharjo, Wijang Wisnu Raharjo, and Bagus H. Jihad. "Stress Analysis of Thick-Walled Cylinder for Rocket Motor Case under Internal Pressure." *Journal of Advanced Research in Fluid Mechanics and Thermal Sciences* 70, no. 2 (2020): 106-115. https://doi.org/10.37934/arfmts.70.2.106115

[4] Al Mayas, A. A., Chen Aolin, Faieza Abdul Aziz, Noorfaizal Yidris, and Kamarul Arifin Ahmad. "Investigation of Solid Propellant Rocket Motor Nozzle via CFD Simulation." *Journal of Advanced Research in Fluid Mechanics and Thermal Sciences* 68, no. 2 (2020): 1-8. https://doi.org/10.37934/arfmts.68.2.18

[5] Beckstead, Merrill W., R. L. Derr, and C. F. Price. "A model of composite solid-propellant combustion based on multiple flames." *AiAA Journal* 8, no. 12 (1970): 2200-2207. https://doi.org/10.2514/3.6087

[6] Lee, Sung-Taick, Edward W. Price, and Robert K. Signan. "Effect of multidimensional flamelets in composite propellant combustion." *Journal of Propulsion and Power* 10, no. 6 (1994): 761-768. https://doi.org/10.2514/3.23813

[7] Hegab, A. M., H. H. Sait, A. Hussain, and A. S. Said. "Numerical modeling for the combustion of simulated solid rocket motor propellant." *Computers & Fluids* 89 (2014): 29-37. https://doi.org/10.1016/j.compfluid.2013.10.029

[8] Raun, R. L., A. G. Butcher, and M. W. Beckstead. "Slope break and high pressure combustion instability." In *28th JANNAF Combustion Subcommittee Meeting Proceedings. Chemical Propulsion Information Agency (CPIA) Publication*, vol. 573. 1991.

[9] Binauld, Quentin, Jean-Michel Lamet, Lionel Tessé, Philippe Rivière, and Anouar Soufiani. "Numerical simulation of radiation in high altitude solid propellant rocket plumes." *Acta Astronautica* 158 (2019): 351-360. https://doi.org/10.1016/j.actaastro.2018.05.041

[10] Sams IV, Oliver C., Joseph Majdalani, and Tony Saad. "Mean flow approximations for solid rocket motors with tapered walls." *Journal of Propulsion and Power* 23, no. 2 (2007): 445-456. https://doi.org/10.2514/1.15831

[11] Toro, Eleuterio F., Michael Spruce, and William Speares. "Restoration of the contact surface in the HLL-Riemann solver." *Shock waves* 4, no. 1 (1994): 25-34. https://doi.org/10.1007/BF01414629

[12] Dombrovsky, Leonid A., and Truc-Nam Dinh. "The effect of thermal radiation on the solidification dynamics of metal oxide melt droplets." *Nuclear engineering and design* 238, no. 6 (2008): 1421-1429. https://doi.org/10.1016/j.nucengdes.2007.10.010

[13] Tseng, Charles C., and Raymond Viskanta. "On the hypothesis of internal phase change." *International communications in heat and mass transfer* 32, no. 10 (2005): 1267-1272. https://doi.org/10.1016/j.icheatmasstransfer.2005.07.004

[14] Godunov, Sergei Konstantinovich. "A difference method for numerical calculation of discontinuous solutions of the equations of hydrodynamics." *Matematicheskii Sbornik* 89, no. 3 (1959): 271-306.

[15] Carlson, Donald J., and Richard F. Hoglund. "Particle drag and heat transfer in rocket nozzles." *Aiaa Journal* 2, no. 11 (1964): 1980-1984. https://doi.org/10.2514/3.2714

[16] Trotter, Hale F. "On the product of semi-groups of operators." *Proceedings of the American Mathematical Society* 10, no. 4 (1959): 545-551. https://doi.org/10.1090/S0002-9939-1959-0108732-6